Ceramics International 50 (2024) 16155–16165

Contents lists available at ScienceDirect

Ceramics International

journal homepage: www.elsevier.com/locate/ceramint

MXene derived TiO_2–ZnO nanocomposites and well-defined n-n heterojunctions for highly efficient lung cancer biomarkers detection

Kaichun Xu [a], Yifan Luo [a,b], Jinyong Xu [a], Zichen Zheng [a], Ahmadou Ly [c], Driss Lahem [c], Marc Debliquy [b], Chao Zhang [a,*]

[a] College of Mechanical Engineering, Yangzhou University, Yangzhou, 225127, PR China
[b] Service de Science des Matériaux, Faculté Polytechnique, University of Mons, Mons, 7000, Belgium
[c] Material Science Department, Materia Nova ASBL, Mons, 7000, Belgium

ARTICLE INFO

Handling Editor: Dr P. Vincenzini

Keywords:
MXene
Heterojunction
Gas sensor
Lung cancer
Isopropanol

ABSTRACT

Enhancing the sensing properties of resistive sensors holds pivotal importance as a non-invasive technology for identifying lung cancer biomarkers. This study focused on the development of a robust sensing platform to effectively detect low-concentration biomarkers with low concentration. $Ti_3C_2T_x$ MXene was prepared by HF etching and ZnO was successfully grown on the MXene nano-multilayers via hydrothermal method subsequently. TiO_2–ZnO samples were obtained after the calcination step. Various characterization methods were applied to validate the structural integrity and formation of the TiO_2–ZnO n-n heterojunction. The TiO_2–ZnO sensor with a Ti:Zn atom ratio of 1:1 (TZ1) exhibited special sensing characteristics, which can be attributed to the higher activation energy (89.2 kJ/mol) and the more substantial interfacial contact areas between the two metal oxides. This architectural arrangement gives rise to the creation of numerous energy barriers, effectively hindering electron migration. Despite exhibiting the acceptable response, TZ1 can be applied in electronic nose systems to effectively detect lung cancer indicators with low concentrations (i.e., acetone, formaldehyde, NH_3) in light of its high stability and steady signal-to-noise ratio.

1. Introduction

The advancement of electronic nose (E-nose) technology has garnered significant attention due to its remarkable integration capabilities and the myriad of sensor options it offers. These attributes make it a promising tool for the swift diagnosis of lung cancer [1–4]. E-nose systems are tasked with processing diverse signals from equipped sensors to analyze complex gas mixtures [5–7]. However, it often struggles to make distinct differentiations, especially when dealing with compounds which have the same functional groups, and this deficiency becomes particularly evident when handling volatile organic compounds (VOCs) and small molecule gases at ultra-low concentrations [8]. Consequently, the development of sensors exhibiting exceptional sensing performance becomes imperative [9]. Zinc oxide (ZnO) is necessary to be modified due to its inherent limitations in selectivity and sensitivity towards low-concentration VOCs and small molecule gases [10–15]. The specific surface area of the sensing material can be significantly enhanced if the metal oxides are uniformly dispersed in the two-dimensional material [16,17]. Current research on two-dimensional composite materials primarily focuses on the effect of graphene, graphene oxide (GO), or reduced graphene oxide (rGO) composited with metal oxide semiconductors (MOSs) [18–21]. However, the composites of GO or rGO, MoS_2, and MOSs usually exhibit a poor response to the low-concentration target gases due to their high interlayer conductivity [22,23]. The emergence of $Ti_3C_2T_x$ MXene as a new breed of two-dimensional material introduces new possibilities [24–26]. $Ti_3C_2T_x$ initially exhibits metal-like interlayer bonding, rendering its resistance insufficient for gas sensing due to its exceptionally high interlayer conductivity, which is usually in the range of 1 kΩ–10 kΩ [26–28]. $Ti_3C_2T_x$ can be transformed into TiO_2 through calcination, which can greatly reduce the interlayer conductivity and retain a high specific surface area [29], thereby creating new reaction sites for VOCs [30].

Song et al. devised a stratified GO-$Ti_3C_2T_x$ MXene-GO coating on Si matrix and oxidized $Ti_3C_2T_x$ into TiO_2 particles integrated between rGO layers by H_2O_2 treatment [31]. This sensor exhibited a robust response (150% @ 1 ppm NO_2) with excellent selectivity at room temperature

* Corresponding author. College of Mechanical Engineering, Yangzhou University, Yangzhou, 225127, Jiangsu Province, PR China.
E-mail address: zhangc@yzu.edu.cn (C. Zhang).

https://doi.org/10.1016/j.ceramint.2024.02.095
Received 26 November 2023; Received in revised form 29 January 2024; Accepted 6 February 2024
Available online 7 February 2024

(RT). Hou et al. prepared the $Ti_3C_2T_x$-derived TiO_2–C/g-C_3N_4 complex by heat treatment at 550 °C, which was used for detecting ppm ethanol at RT with the ultraviolet light activating [32]. The sensor performed a 90% response to 10 ppm ethanol, which is about 10 times higher than the normal TiO_2/g-C_3N_4. However, it also exhibited a high response to benzene and methanol, implying the poor selectivity of the sensor. Zhou et al. prepared N-doped $Ti_3C_2T_x$ by hydrothermal method through adding urea and $Ti_3C_2T_x$ powder into glycol solution [33]. With the hydrothermal reaction time extending, the number of TiO_2 particles on the surface increased, and a $Ti_3C_2T_x$/TiO_2 composite was formed. The response of the $Ti_3C_2T_x$/TiO_2 sensor to 1 ppm NH_3 reached 24.5% at RT with a limit of detection (LOD) of 200 ppb. Tian et al. grew MoS_2 nanosheets on $Ti_3C_2T_x$ by the hydrothermal method [34]. Part of the $Ti_3C_2T_x$ on the surface was oxidized, and TiO_2 particles were formed in the hydrothermal reaction. The sensor showed excellent response to ppm-level NH_3 with a LOD of 500 ppb. Wen et al. prepared thin TiO_2 nanosheets by heat treatment of $Ti_3C_2T_x$ MXene at 400 °C and modified Ag on the obtained TiO_2 by annealing the mixture of TiO_2 and $AgNO_3$ solution [35]. The sensor showed an impressively superior response to NH_3 (200% @ 5 ppm) at a relative humidity (RH) of 90%.

Herein, we combined the $Ti_3C_2T_x$-derived TiO_2 with ZnO and proposed a feasible approach to enhance gas sensing properties. $Ti_3C_2T_x$-derived TiO_2 remains the two-dimensional sheet structure which lead to a considerable specific surface area, thus increases the electrical resistance and facilitates the formation of the heterojunctions with ZnO particles. This junction effectively minimized the electrical noise of the sensor [36]. In this work, after etching with a hydrogen fluoride (HF) solution, multi-layer $Ti_3C_2T_x$ was prepared by centrifugation and high-speed agitation. Subsequent growth of ZnO nanoparticles on the surface of $Ti_3C_2T_x$ was facilitated by the connection between the electronegative surfaces of Zn^{2+} and $Ti_3C_2T_x$ through the cationic surfactant CTAB. Subsequently, the complex was annealed at 500 °C to mitigate the short-circuit effect caused by its high interlayer conductivity. The role of TiO_2 on the sensitivity and selectivity of ZnO sensors was evaluated through low-concentration VOCs sensing experiments. When the molar ratio of ZnO to TiO_2 was close, a substantial quantity of heterojunction structures emerged at the interface between these two materials. This hindered electron transport, leading to a relatively diminished response value. Furthermore, despite the decrease in response value following the amalgamation of ZnO and TiO_2, TiO_2/ZnO heterostructures with $Ti_3C_2T_x$ MXene-layer structure exhibited an elevated signal-to-noise ratio (SNR) and excellent detection capability for low concentrations of isopropyl alcohol over a wide temperature range, which may shed light on constructing MOS-based gas sensors applied in health administration with a high SNR.

2. Experiment

2.1. Preparation of $Ti_3C_2T_x$

The $Ti_3C_2T_x$ MXene was obtained by exfoliating commercial MAX (Ti_3AlC_2) powders (≥90%, ≤40 μm) purchased from Sigma Aldrich. To achieve this, 5% hydrofluoric acid (HF) was added into a Teflon autoclave, and 1 g of MAX powders were slowly added into the acid solution and magnetically stirred at 35 °C for 24 h. After etching, the obtained black powders were centrifuged and washed by DI-water and ethanol at 3000 rpm until the pH of the supernatant was over 6. After washing, the suspension was mechanically agitated by a vortex agitator at a speed of 4000 rpm for 1.5 h. The $Ti_3C_2T_x$ powders were kept in 25 mL of water as a precursor.

2.2. Synthesis of samples

0.2 g of Cetyl trimethyl ammonium bromide (CTAB) was completely dissolved into 22 mL of ethanol, and x mL of the as-prepared $Ti_3C_2T_x$ suspension was slowly added into the CTAB solution with stirring for

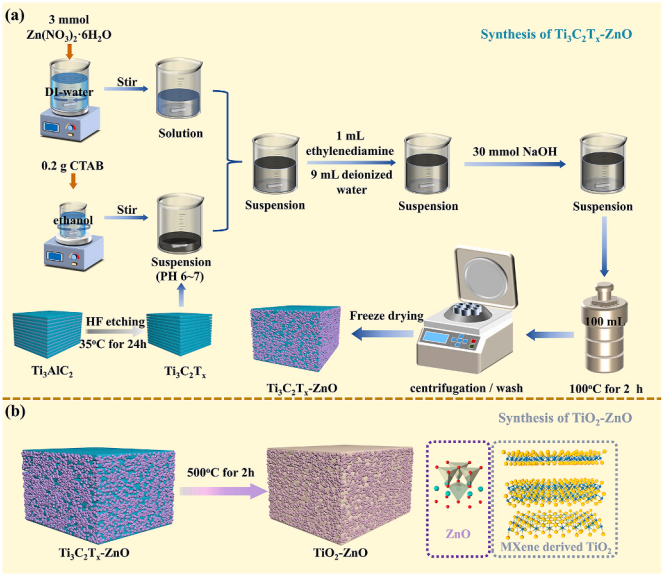

Fig. 1. Schematic diagram of synthesis process of (a) MXene-ZnO and (b) TiO_2–ZnO.

over 30 min. In parallel, 3 mmol of $Zn(NO_3)_2{\cdot}6H_2O$ were dissolved in 44-x mL of DI-water. The two solutions were mixed together when both of them became uniform. After 15 min of stirring, 30 mmol of NaOH was added and mixed into the solution. Simultaneously, a mixture of 1 mL of ethylenediamine and 9 mL of DI water was introduced. The resultant solution was transferred into a Teflon-lined autoclave and reacted at 100 °C for 2 h. In order to investigate the impact of the ratio between ZnO and $Ti_3C_2T_x$ on gas sensing properties, four different $Ti_3C_2T_x$-ZnO samples were prepared by changing the x as 0, 2.5, 5, 10, and 15. The four samples are named as ZnO, MZ0.5, MZ1, MZ2, and MZ3, respectively.

Given $Ti_3C_2T_x$'s inherent conductivity, it is advisable to transform $Ti_3C_2T_x$ into TiO_2 through a calcination process for sensor applications. The $Ti_3C_2T_x$-ZnO samples and pure $Ti_3C_2T_x$ were calcined in a muffle furnace at 500 °C for 2 h (5 °C/min). The obtained light grey powders were named as TZ0.5, TZ1, TZ2, TZ3, and $Ti_3C_2T_x$-TiO_2. Fig. 1(a and b) exhibit the synthesis process of $Ti_3C_2T_x$-ZnO and TiO_2–ZnO.

2.3. Material characterization

The morphologies of $Ti_3C_2T_x$, $Ti_3C_2T_x$-ZnO, and TiO_2–ZnO samples were observed by FE-SEM (SU8020, Hitachi), and the element ratios of MZ1 and TZ1 were measured by EDS (S4800II, Hitachi). XRD tests were carried out on $Ti_3C_2T_x$, $Ti_3C_2T_x$-ZnO, and all TiO_2–ZnO samples (D8 Advance, Bruker) with a $CuK_{\alpha1}$ radiation source (λ = 1.5418 Å). The scanning speed is 0.2 s/step, and the scanning range is 5° to 80°. HRTEM was applied to test MZ1 and TZ1 for further verifying the combination of TiO_2 and ZnO (Tecnai G2 F30 S-TWIN, FEI). XPS was employed to analyze the valence states and defect concentrations of $Ti_3C_2T_x$-derived TiO_2, $Ti_3C_2T_x$-ZnO, TiO_2–ZnO, ZnO (PHI Versa Probe 5000, Ulvac-Phi), and the X-ray source is monochromatic AlK_{α} radiation with a power of 50 W and a ray voltage of 15000 V. The pressure in the test chamber is about 1×10^{-9} Torr.

2.4. Gas sensing measurement

The prepared samples were mixed with 1 mL of DI-water to form a slurry, and sensors were fabricated by applying the slurry to the sensor matrix. The TZ-based sensors fabricated were aged at 350 °C for 72 h to stabilize the resistance signal. The sensing set-up was consisted of a gas supply system, mass-flow controllers, signal collecting device, and

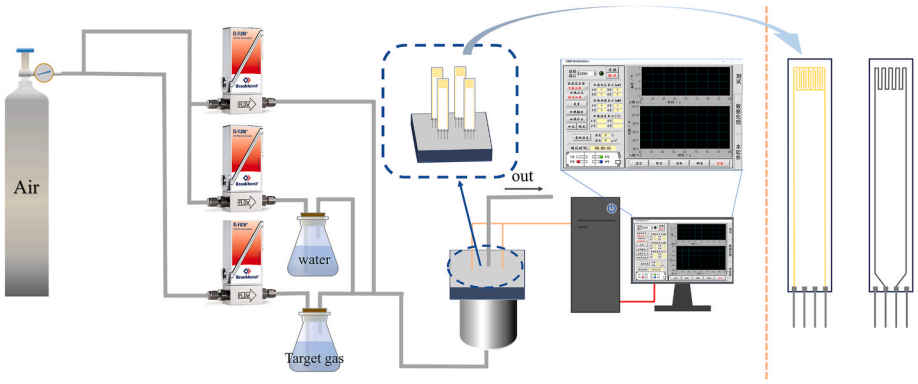

Fig. 2. The set-up of gas sensing measurement.

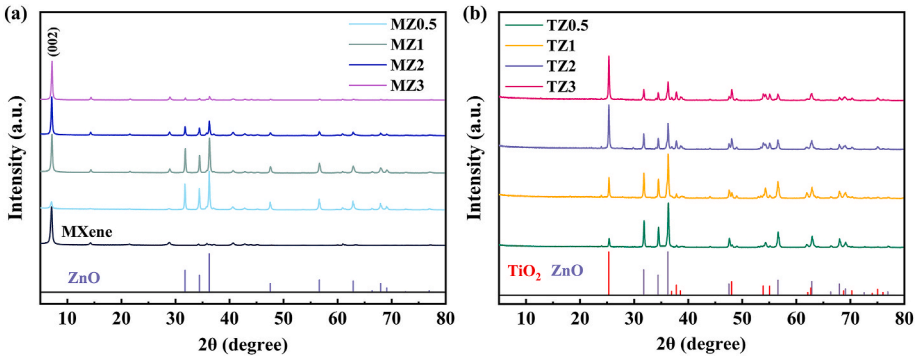

Fig. 3. XRD patterns of (a) MXene and MXene-ZnO samples and (b) TiO_2–ZnO samples.

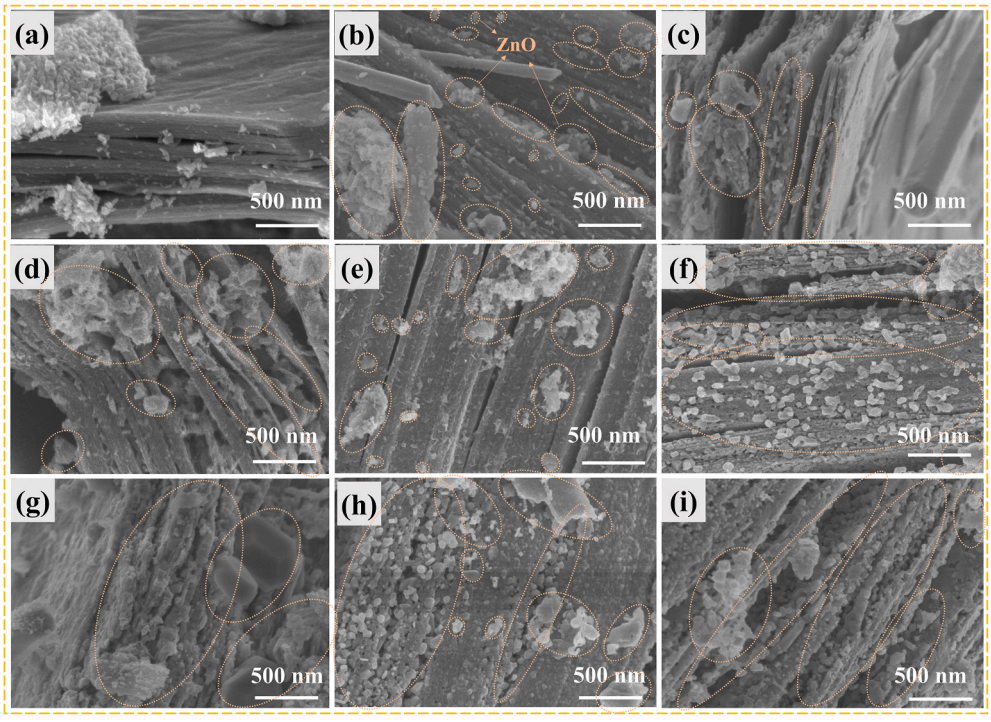

Fig. 4. (a) The SEM images of (a) MXene, (b) MZ0.5, (c) MZ1, (d) MZ2, (e) MZ3, (f) TZ0.5, (g) TZ1, (h) TZ2, and (i) TZ3.

sensors (Fig. 2). The detailed information of sensor matrix and gas sensing device were provided in supporting information. The RH and concentration of VOCs were controlled by three mass-flow controllers. The response was defined as $S=(R_a-R_g)/R_g \times 100\%$ because the resistance decreased as reducing gas was filled into the gas chamber (R_a and R_g represented the resistance stable in air and target gas, respectively). The response/recovery time was defined as the time it takes for the resistance to decrease to R_a-90% × (R_a-R_g) and to recover to R_a-10%

Table 1
Element quantity of MZ1 measured by EDS.

Element	Weight ratio (%)	Atom ratio (%)
C	11.71	27.88
O	17.45	31.20
F	5.29	7.96
Al	0.36	0.38
Ti	25.46	15.21
Zn	39.73	17.37

Table 2
Element quantity of TZ1 measured by EDS.

Element	Weight ratio (%)	Atom ratio (%)
C	0.38	0.45
O	27.98	55.38
F	0.56	0.94
Al	0.38	0.45
Ti	27.03	17.89
Zn	42.19	20.43

× (R_a-R_g), respectively.

3. Result and discussion

3.1. Material characterizations

To explore the effective oxidation of $Ti_3C_2T_x$ to TiO_2 during both the synthesis stage of ZnO and the heat treatment process, the phase of prepared $Ti_3C_2T_x$-ZnO and TiO_2–ZnO were confirmed by XRD. The XRD spectra of the MZ samples exhibited characteristic peaks of $Ti_3C_2T_x$ (002) and diffraction peaks related to hexagonal ZnO (JCPDS 65–3411), indicating that $Ti_3C_2T_x$ was hardly oxidized during the hydrothermal reaction process (Fig. 3a). Additionally, with an increase in the amount of $Ti_3C_2T_x$ suspension added, the characteristic peak of $Ti_3C_2T_x$ (002) at around 7° significantly increased. In all TZ samples, there were no characteristic peaks in the range of 5–10°, and all diffraction peaks corresponded to hexagonal ZnO and rutile TiO_2 (JCPDS 71–1167) (Fig. 3b). The results confirm the complete conversion of $Ti_3C_2T_x$ to TiO_2 during the heat treatment process.

SEM image of $Ti_3C_2T_x$ was shown in Fig. 4a, which indicated that the HF solution successfully separated the MAX bulks into multi-layered $Ti_3C_2T_x$ pieces. Certain tiny particles (oval dotted line) can be discerned on the surface of $Ti_3C_2T_x$ nano-multilayers or in between the exfoliated layers (Fig. 4(b–e)). During the synthesis of $Ti_3C_2T_x$-ZnO, CTAB, a cationic surfactant, was used as the ligand between the negatively charged surfaces of $Ti_3C_2T_x$ and Zn^{2+} in the solution [37]. Thus, these particles could be attributed to two potential materials: TiO_2 derived from $Ti_3C_2T_x$ or ZnO particles grown on the surface. The particle size distribution histogram indicates that following heat treatment at 500 °C, there is an increase in particle size attributed to the elevated temperature, providing the necessary energy for ZnO crystal growth (Fig. S1). Moreover, the layered structure of $Ti_3C_2T_x$ was preserved without being destroyed, as shown in Fig. 4(f–i).

EDS tests of MZ1 and TZ1 powders were carried out to further understand the elements on the surface, as shown in Tables 1 and 2. The atomic ratio of Zn to Ti was very close, and the Al content was nearly 0, indicating that Al layers in the MAX phase had been dissolved and removed by HF. Additionally, the F content decreased further after calcination. The corresponding mapping selection regions were shown in Fig. 5(a–h), respectively, and the mapping results of MZ1 and TZ1 were shown in Fig. 5(b–g) and 5(i-n). It's evident that the majority of Al originated from the platform used to hold the powders, while C primarily derived from the tapes employed in the preparation of SEM samples. Importantly, ZnO effectively grew on the $Ti_3C_2T_x$ nanolayers, and before the calcination, the $Ti_3C_2T_x$ had been partially oxidized during the hydrothermal step. The primary distribution position of Zn in the mapping image was basically consistent with that of Ti, which implies that ZnO was successfully attached to the surface of $Ti_3C_2T_x$ and TiO_2 in the synthesis process and that most of Al had been removed during the etching process. In the etching step, some F^- coming from the HF solution was bonded to the surface of $Ti_3C_2T_x$, which was not completely removed from the surface after heat treatment.

TEM image of MZ1 implied that ZnO was successfully grown on the $Ti_3C_2T_x$ layer (Fig. 6a), and the HRTEM image exhibited the

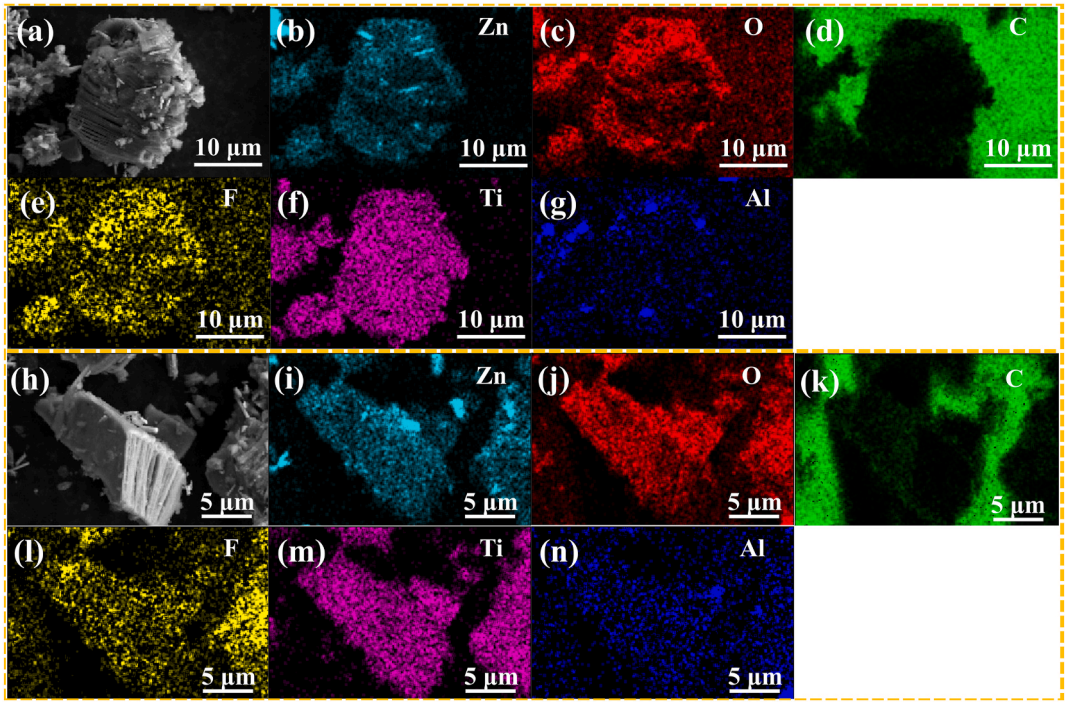

Fig. 5. The selected region of (a) MZ1 and (h) TZ1; the mapping results of (b–g) MZ1 and (i–n) TZ1.

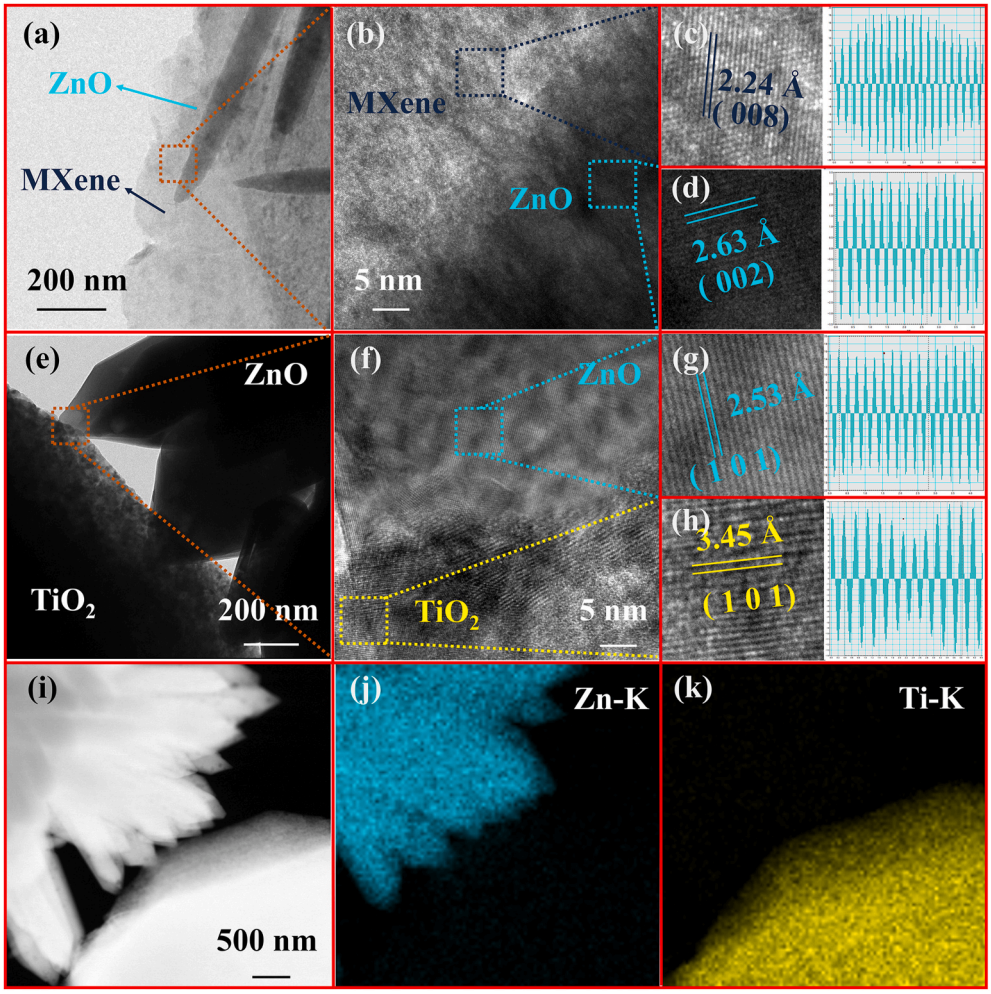

Fig. 6. (a) TEM and (b) HRTEM of MZ1; (c) MXene region and (d) ZnO region of HRTEM images of MZ1; (e) TEM and (f) HRTEM of TZ1; (g) ZnO region and (h) TiO_2 region of HRTEM images of TZ1; (i–k) mapping of TZ1.

heterojunction region of ZnO/$Ti_3C_2T_x$ (Fig. 6b), where the lattice bands of ZnO (002) and $Ti_3C_2T_x$ (008) are visual (Fig. 6(c and d)). The TEM image of ZnO/TiO_2 were visually depicted in Fig. 6e. There are obvious boundaries between the upper and lower parts in Fig. 6f. The upper section corresponded to ZnO, while the lower region was associated with TiO_2. Fig. 6(g and h) exhibit the local amplification images of the two parts in Fig. 6f, and the distances of the lattice bands were 2.53 Å and 3.45 Å, which were corresponding to the ZnO (101) and TiO_2 (101) crystal faces, respectively. It is intuitive that the Zn and Ti elements were distributed on both sides, indicating that Ti atoms did not diffuse during the hydrothermal synthesis of ZnO or calcination, as illustrated in Fig. 6 (i–k).

To assess the element ratios between Ti and Zn and the removal of C and Al from the composites, XPS tests were performed on the $Ti_3C_2T_x$-ZnO and TiO_2–ZnO samples. Fig. 7(a–e) exhibit the survey, O 1s, Zn 2p, and Ti 2p regions of all samples. C, O, Zn, Ti, and F can be observed in the survey spectra of all the MZ and TZ samples. In the case of MZ1, C peaks were fitted into three different peaks at 284.7 eV, 286.5 eV, and 288.8 eV, representing C–C bonds, C–O bonds, and C═O bonds [38], respectively, indicating that part of C was related to the $Ti_3C_2T_x$, as shown in Fig. 7f. Ti and Zn were attributed to the $Ti_3C_2T_x$ multilayers and ZnO nanoparticles, respectively. The F in the samples was linked to the etching step of the MAX phase, with some F^- from the solution adsorbed on the surface of $Ti_3C_2T_x$, which is in accordance with the F peak related to the metal fluoride bond. While in TZ samples, the atom ratio of C decreased significantly and only peaks related to the C pollution remained, which indicated that C in the $Ti_3C_2T_x$ structure was successfully removed and turned the structure into TiO_2. In addition, the survey, Ti 2p, Zn 2p, and O 1s regions of $Ti_3C_2T_x$-TiO_2 and ZnO are shown in Fig. 7(g–l). Furthermore, based on the semi-quantitative XPS analysis results, in the four sets of TiO_2–ZnO samples, the atomic ratios of Ti to Zn were calculated to be approximately 13.1:23.3, 16.8:18.2, 20.9:9.8, and 24.5:8.8, respectively. These ratios closely aligned with the Ti:Zn ratios set during the preparation process, indicating that almost all of the $Ti_3C_2T_x$ transformed into TiO_2 after the heat treatment.

3.2. Gas sensing performance

The optimal operating temperature of the sensors was first ascertained to further evaluate the sensing performances of the fabricated sensors. Due to the high interlayer conductivity of $Ti_3C_2T_x$, MZ samples exhibited low resistance, which is detrimental to the gas sensing performance of n-type MOSs. Meanwhile, MZ samples are not suitable for isopropanol detection due to their poor stability under high working temperature. To provide a specific explanation, MZ-based sensors were prepared following the fabrication method of TZ-based sensors but stabilized for 7 days at room temperature. Fig. S2 illustrates the dynamic response characteristics of MZ samples to 5 ppm isopropanol at 225–375 °C. With an increase in the amount of added $Ti_3C_2T_x$, the baseline resistance of the MZ-based sensor significantly decreased at low temperatures. As the temperature rose, $Ti_3C_2T_x$ was gradually oxidized to TiO_2 at high temperatures, creating more energy barriers and leading

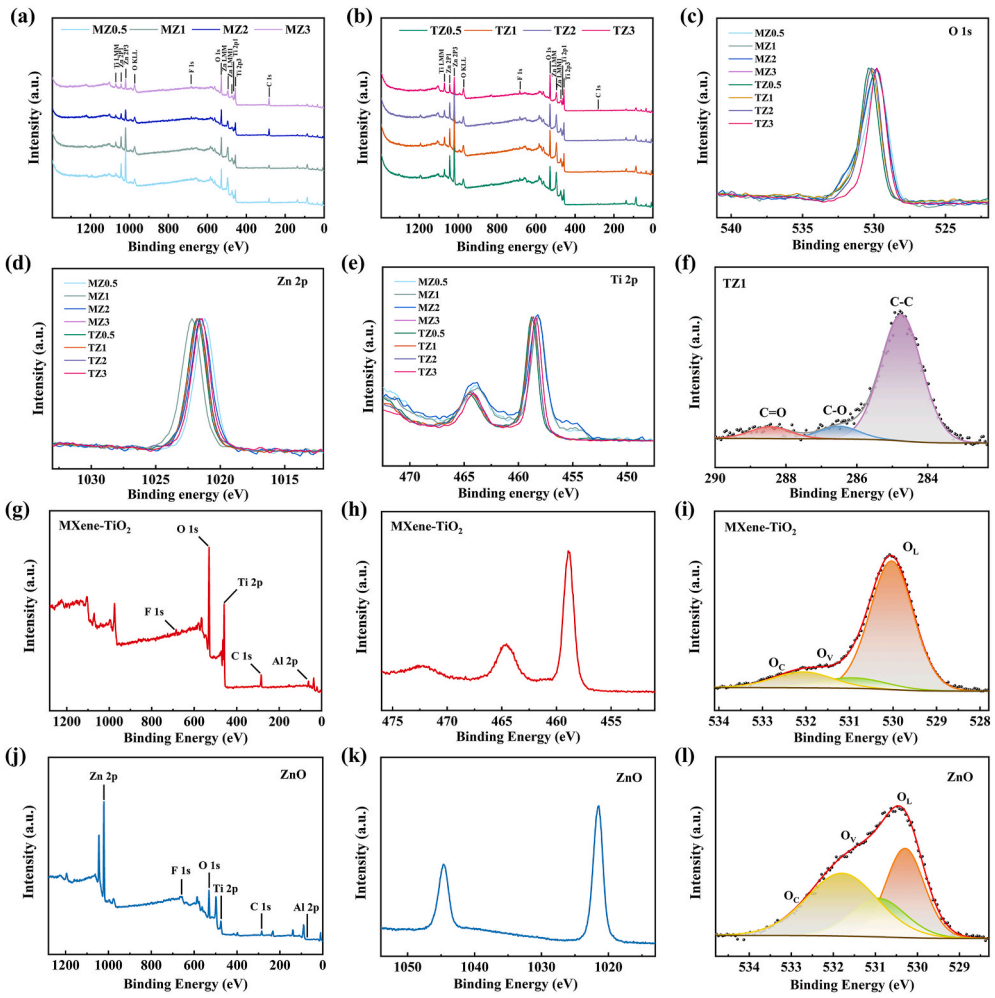

Fig. 7. XPS survey spectra of (a) MZ and (b) TZ samples; (c) O1s region, (d) Zn 2p region, and (e) Ti 2p region of MZ and TZ samples; (f) C1s region of TZ1; (g) survey, (h) Ti 2p region, and (i) O1s region of MXene-TiO_2; (j) survey, (k) Zn 2p region, and (l) O1s region of ZnO.

to a continuous increase in the baseline resistance of MZ samples at high temperatures. As the amount of added $Ti_3C_2T_x$ was relatively low, the TiO_2/ZnO in the MZ samples accounted for a certain proportion after the operating temperature reached 300 °C. The further enhancement of operating temperature contributed to a dominant effect of decreased resistance due to the rise in carrier concentration, outweighing the increase caused by $Ti_3C_2T_x$ oxidation. Consequently, we proceeded to study the sensing characteristics of TZ samples.

The response values of all TZ-based sensors to 5 ppm isopropanol at 50% RH from 225 °C to 375 °C were shown in Fig. 8a. The four TiO_2–ZnO sensors exhibited distinct sensing behaviors. For the TZ0.5 sensor, the highest response occurred at 275 °C, and the response value was much higher than that at the other temperature, which has the same optimal temperature as ZnO (Fig. 8b). Subsequently, the behavior of the TZ3 sensor was quite similar to that of the $Ti_3C_2T_x$-derived TiO_2 sensor (Fig. 8b), with an optimal working temperature in a relatively lower temperature range. The response value of the TZ2 sensor was insufficient for meaningful analysis. The TZ1 sensor exhibited intriguing behavior as the temperature increased. In contrast to the TZ0.5 and TZ3 sensors, the TZ1 sensor demonstrated its highest response in the high-temperature range, with the optimal working temperature at 350 °C, which was much higher than both ZnO and TiO_2 sensors. Another notable difference was observed in the response range between the highest and lowest values, which was defined as $(S_{max}- S_{min})/S_{max}$ (S_{max} and S_{min} referred to the highest and lowest response values, respectively). For TZ0.5, the difference was 68.0%, while the value for TZ3 was 68.8%. The difference of TZ1 was 21.5%, which should be attributed to the potential barrier generated at the boundary of TiO_2 and ZnO. The TZ1 sensor was significantly different from the other three sensor groups due to its similar TiO_2-to-ZnO ratio, resulting in more contact areas between the two metal oxides and the formation of numerous barriers that hindered electron migration. Additionally, electron depletion and accumulation layers were formed on both sides of the junction region, respectively, resulting in a reduction in the number of surface free carriers. Consequently, higher operating temperatures were required to excite more carriers. Thus, TZ1 could provide a relatively high response and a significantly distinct signal compared to other sensors. Considering its unique characteristics, TZ1 was selected as the target sensor in the subsequent test, aligning with our application requirements.

The response behavior of TZ sensors to 5 ppm isopropanol, 5 ppm acetone, 5 ppm formaldehyde, and 50 ppm ammonia were studied at 350 °C with 50% RH to qualify the selectivity change (Fig. 8c). The selectivity trend could be divided into two parts. TZ0.5 and TZ1 sensors showed similar selectivity, and their response values to isopropanol and formaldehyde were nearly identical, while their responses to 5 ppm acetone and 50 ppm NH_3 were slightly lower and showed similar values. For the TZ2 and TZ3 sensors, they both exhibited the best response to acetone, and the minor difference between them was that the TZ2 had an excellent selectivity for formaldehyde and acetone, while the TZ3 was more sensitive to isopropanol and acetone.

The dynamic resistance and response curves of the TZ1 sensor to various concentrations (5 ppm–250 ppb) of isopropanol at 350 °C are

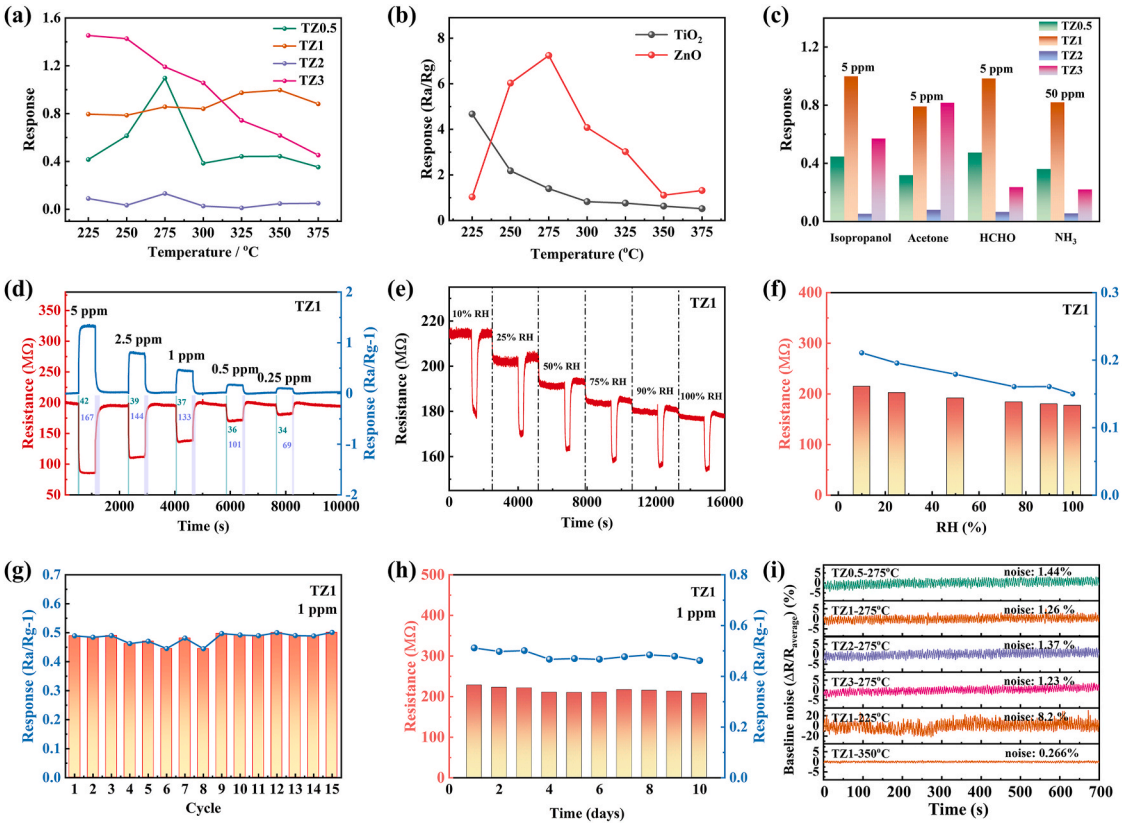

Fig. 8. (a) Response of different TiO_2–ZnO sensors to 5 ppm isopropanol with 50% RH at different operating temperature; (b) response of MXene-TiO_2 and ZnO sensors to 5 ppm isopropanol with 50% RH at different operating temperature; (c) response of TiO_2–ZnO sensors to lung cancer biomarkers at 350 °C with 50% RH; (d) dynamic resistance and response curve of TZ1 sensor to isopropanol with various concentrations from 5 ppm to 0.25 ppm with 50% RH at 350 °C; (e) electrical resistance curves and (f) baseline resistance and response value to 500 ppb isopropanol at 350 °C with various RH; (g) repeatability, (h) long-term stability of the TZ1 sensor with 50% RH to 1 ppm isopropanol at 375 °C; (i) baseline resistance noises of sensors stabilized in air atmosphere.

Table 3
Comparison of sensing performance of TZ-based sensors and other n-type sensors.

Material	Target gas	Concentration (ppm)	Operating temperature (°C)	Response (R_a-R_g)/R_g × 100%)	Response/recover time (s)	Reference
$MoO_3/TiO_2/Ti_3C_2T_x$	isopropanol	50	RT	245	100/40	[30]
TiO_2/Ti_3C_2T	NH_3	10	RT	3.1	60/750	[39]
TiO_2	Acetone	200	400	750	240/180	[40]
NiO/TiO_2	Acetone	200	400	933	–	[41]
Ag–In_2O_3/ZnO	formaldehyde	100	300	7.4	–	[42]
Graphene/Cu@ZnO	isopropanol	100	270	~400	–	[43]
TZ1	isopropanol	5	350	134.38	42/267	This work

shown in Fig. 8d. The sensor showed typical n-type semiconductor behavior, with electrical resistance decreasing as reducing gas was injected. The response value to 5 ppm isopropanol were 134.38% with the fast response/recovery rate of 42 s/267 s, respectively. The decrease in the concentration of isopropanol led to a reduction in the response/recovery time, attributed to a lower amount of charge transfer (Fig. 8d). Although the response value decreased to 10.56% as the isopropanol concentration decreased to 250 ppb, the SNR remained excellent because of the clear and easily distinguishable resistance change, confirming the sensor's capability to detect 250 ppb isopropanol. Table 3 exhibits the sensing performance of various ZnO or TiO_2-based sensing materials for NH_3, formaldehyde, acetone, and isopropanol, indicating the superior sensing characteristics of TZ1 for isopropanol.

The response of the TZ1 sensor to 500 ppb isopropanol at 350 °C was tested with the RH varying from 10% to 100% to study the role of RH (Fig. 8e). The adsorption of H_2O molecules is physical adsorption without electron transfer, so less oxygen adsorption leads to less electron transfer with the sensing layer, indicating the competitive adsorption of H_2O and O_2 molecules. Thus, the baseline resistance of the TZ1 sensor decreased with the increase in RH. For the response, the value did not significantly decrease with RH increasing, and the absolute value changed from 21% to 15% from 10% RH to 100% RH, representing a 28.6% difference (Fig. 8f).

To assess the repeatability of the sensors, 15 different cycles of testing with 1 ppm isopropanol and 50% RH were conducted after a stable period of 30 h to ensure the sensor's baseline stability. The average response of the 15 tests was 48.17% with a standard deviation of 1.80% (Fig. 8g). The maximum and minimum values were 50.10% (cycle 15) and 44.47% (cycle 8). Moreover, the long-term stability of TZ1 in 10 days was measured, and the average response of 10 testing results was 48.78% with a standard deviation of 1.68% (Fig. 8h). Thus, the repeatability and long-term stability of TZ1 were verified.

Furthermore, noise based on different sensors was visible in the process of detecting the resistance in the air, and the temperature significantly influenced the noise. To quantitatively reflect the noise of each sensor, the baseline noise was defined as (R_{max}-R_{min})/$R_{average}$ [36].

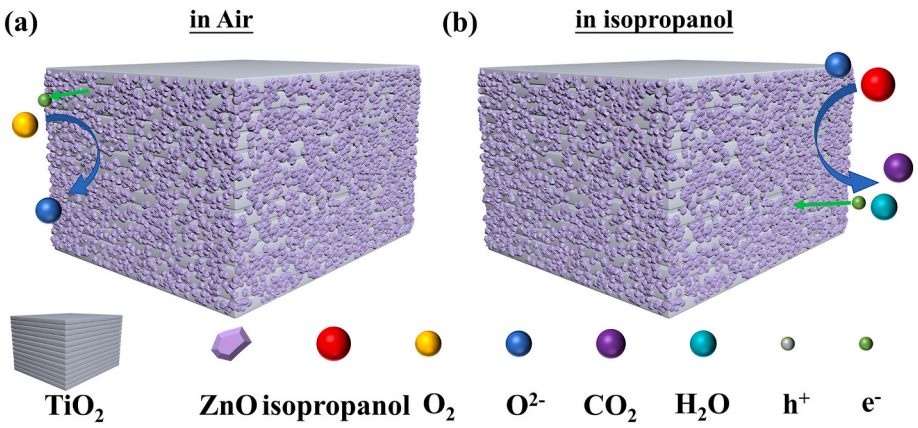

Fig. 9. The schematic of sensing mechanism (a) in Air and (b) in isopropanol.

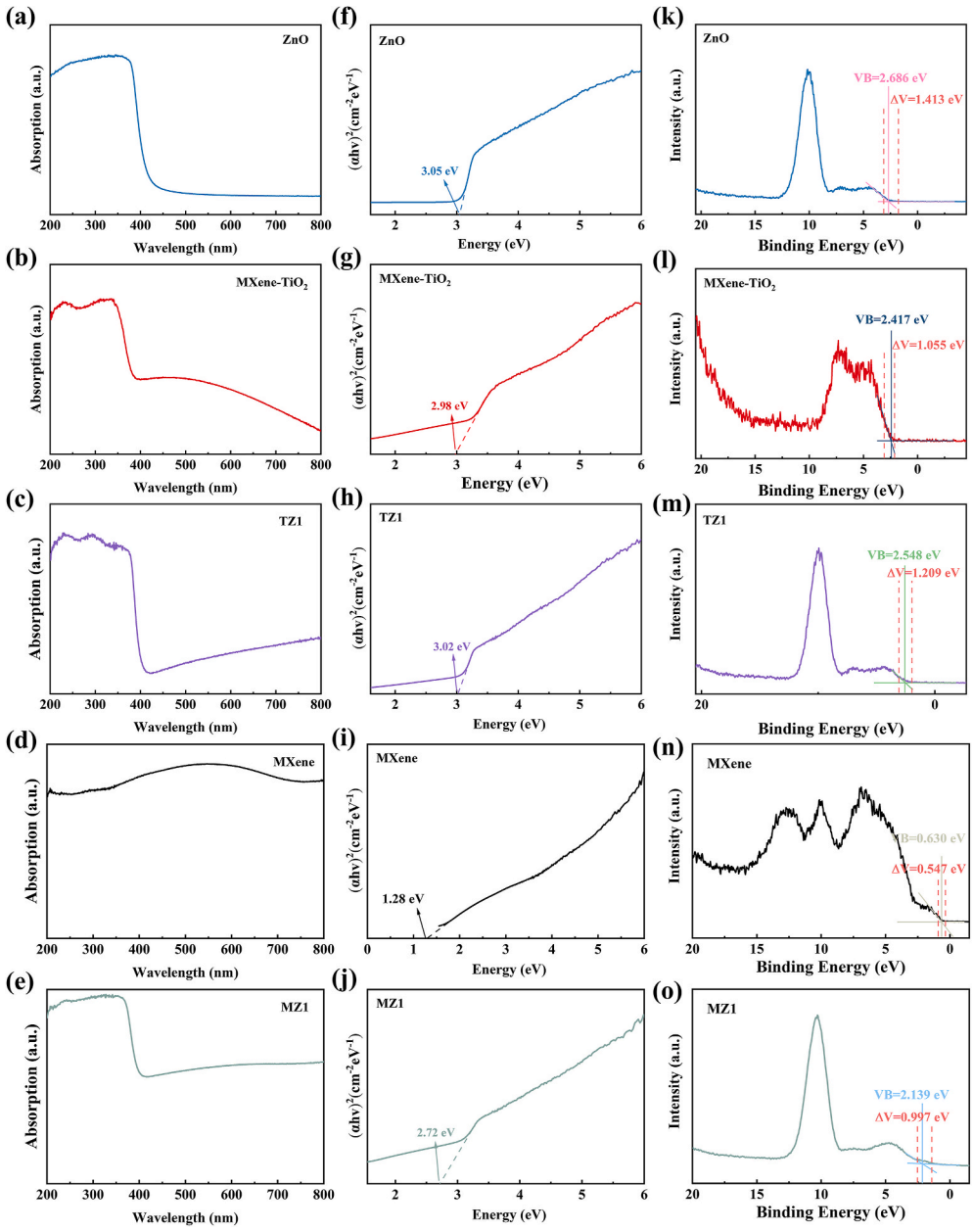

Fig. 10. (a–e) UV–Vis plots, (f–j) Tauc calculation, and (k–o) VB-XPS spectra of ZnO, MXene-TiO_2, TZ1, MXene, and MZ1.

Table 4
The band structure of ZnO, MXene-TiO_2, and TZ1.

Sample	E_g (eV)	$E_{VB,\ XPS}$ (eV)	ΔV (eV)	$E_{VB,\ NHE}$ (eV)	$E_{CB,\ NHE}$ (eV)	Φ (eV)
ZnO	3.05	2.686	1.413	2.766	−0.284	5.933
MXene-TiO_2	2.98	2.417	1.055	2.497	−0.483	5.575
TZ1	3.02	2.548	1.209	2.628	−0.392	5.729
$Ti_3C_2T_x$	1.28	0.630	0.547	0.710	−0.570	5.067
MZ1	2.72	2.139	0.997	2.219	−0.501	5.517

As shown in Fig. 8i, the baseline noises of TZ0.5, TZ1, TZ2, and TZ3 at 275 °C were 1.44%, 1.26%, 1.37%, and 1.23%, respectively. Moreover, the baseline noises of TZ1 at 225 °C and 350 °C were 8.26% and 0.266%, implying that the baseline noise decreased with the operating temperature increasing, which indicated the excellent SNR of TZ1 at the optimal operating temperature (350 °C).

3.3. Gas sensing mechanism

As the sensors were in synthetic air, O_2 molecules adsorbed on the surface of the sensing layer, capturing free electrons from the sensing layer, generating adsorbed oxygen ions, leading to an increase in electrical resistance. At the operating temperature, the oxygen ions were in two different forms (Eqs. (1)–(3), Fig. 9a) [44]. When the target gases were injected, these gases reacted with the adsorbed oxygen, releasing electrons back to the sensing layer and decreasing the electrical resistance. Taking isopropanol as an example, the general reaction on the surface can be written as Eqs. (4) and (5) (Fig. 9b) [32,45].

$$O_{2(gas)} \rightarrow O_{2(ads)} \quad (1)$$

$$O_{2(ads)} + 2e^- \rightarrow 2O^- \ (200-300^oC) \quad (2)$$

$$O_{2(ads)} + 4e^- \rightarrow 2O^{2-} \ (300-375^oC) \quad (3)$$

$$9O^- + CH_3CHCH_3OH \rightarrow 3CO_2 + 4H_2O + 9e^- \quad (4)$$

$$9O^{2-} + CH_3CHCH_3OH \rightarrow 3CO_2 + 4H_2O + 18e^- \quad (5)$$

To further investigate the effect of the formation of n-n heterojunctions of TiO_2–ZnO, the band structures of ZnO, $Ti_3C_2T_x$-TiO_2, TZ1, $Ti_3C_2T_x$, and MZ1 were studied utilizing UV–Vis and VB-XPS. The absorption wavelength of the three samples is about 400 nm, and the band gaps of ZnO, $Ti_3C_2T_x$-TiO_2, TZ1, and MZ1 were determined to be 3.05 eV, 2.98 eV, 3.02 eV, and 2.72 eV, which was relatively close. The band gap of TZ1 was not reduced as the ZnO was grown on the $Ti_3C_2T_x$-derived TiO_2 nanolayers but instead was maintained at a high level of approximately 3 eV, as illustrated in Fig. 10(a–j). The VB-XPS results exhibited the $E_{VB,\ XPS}$, and ΔV of five samples, as shown in Fig. 10(k–o). According to Eqs. (6) and (7) [46], the band structures of five samples were obtained, as shown in Table 4.

$$E_{VB,NHE} = \varphi + E_{VB,XPS} - 4.44 \quad (6)$$

$$\Delta V = \Phi - \varphi \quad (7)$$

Where φ, $E_{VB,\ XPS}$, and ΔV represent the work function of the XPS analyzer (4.52 eV), the valence band potential calculated from VB-XPS, and the potential difference.

The work function values (Φ) of ZnO were determined to be 5.933 eV, which is higher than that of $Ti_3C_2T_x$ MXene (5.067) and TiO_2 (5.575 eV). After contact, free electrons transferred from the CB of TiO_2 and $Ti_3C_2T_x$ MXene to the CB of ZnO until the Fermi levels became equal

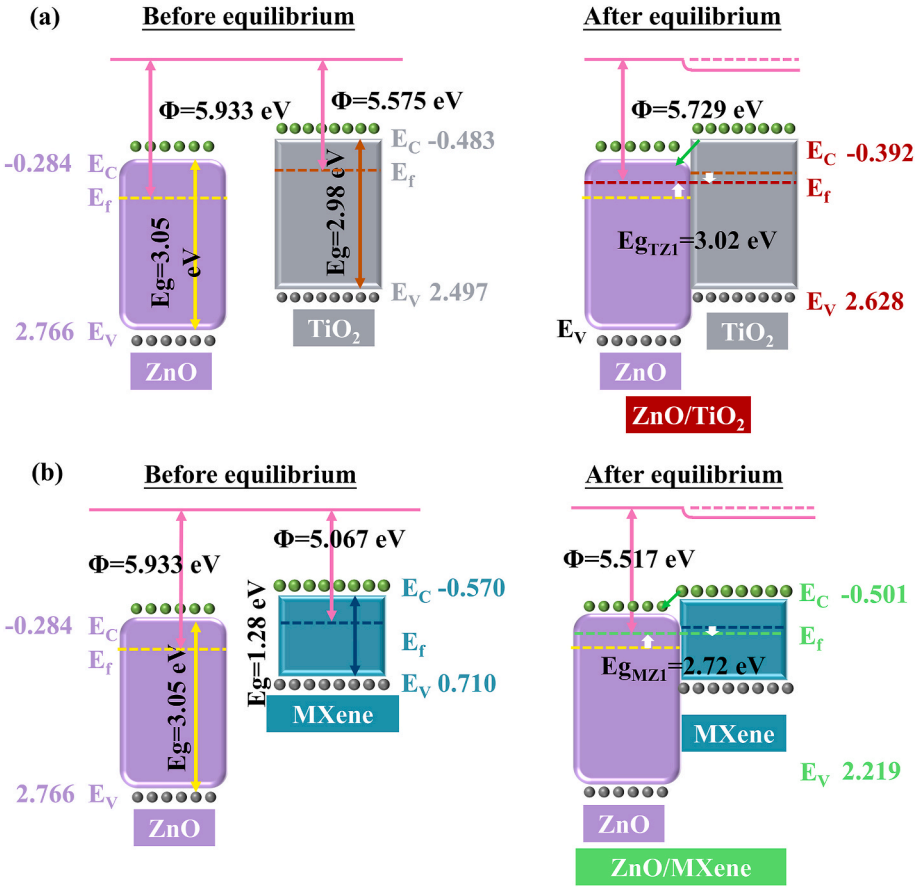

Fig. 11. The band structure of (a) TZ1 and (b) MZ1.

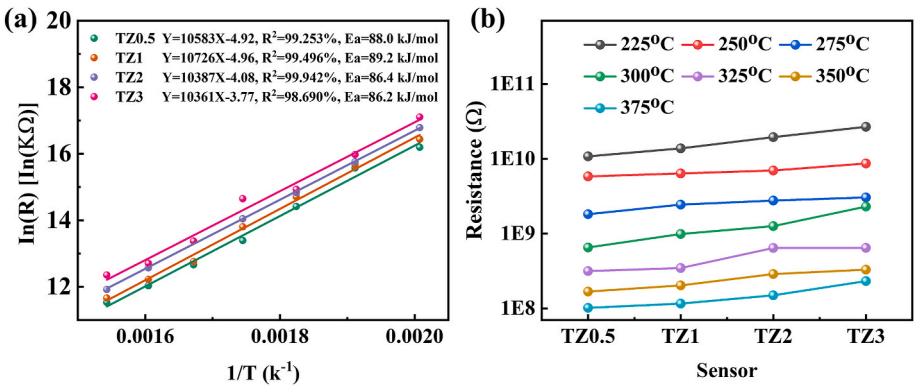

Fig. 12. (a) Arrhenius plots for TZ0.5, TZ1, TZ2, and TZ3 sensors in the air; (b) The resistance value of TZ0.5, TZ1, TZ2, and TZ3 sensors at various working temperatures.

(Fig. 11). In this process, depletion layers and accumulation layers were generated on the two sides of the interfaces and Φ of TZ1 and MXene were 5.729 eV and 5.517 eV, which effectively separated the electron-hole pairs. Consequently, $E_{CB,\ NHE}$ and $E_{VB,\ NHE}$ of TZ1 were −0.392 eV and 2.628 eV, and that of MZ1 were −0.501 eV and 2.219 eV, which indicates that $E_{CB,\ NHE}$ and $E_{VB,\ NHE}$ decreased because of the incorporation of TiO_2 and MXene, implying a lower energy for adsorption and reaction between the target gas and TZ1, which may enhance the response of TZ1 to isopropanol. MZ samples are not suitable for isopropanol detection at high temperatures. Thus, we further investigated the activation energy of TZ samples. The decreased response of TZ1 can be attributed to the highest activation energy (E_a = 89.2 kJ/mol) of TZ1, calculated by Eq. (8) [47], as shown in Fig. 12a.

$$\ln(R) = \ln(R_0) + \left(\frac{E_a}{k_B}\right)\frac{1}{T} \tag{8}$$

Where R, k_B, and T represent the resistance of the sensor stable in air (Ω), the Boltzmann constant 8.317 kJ/(mol·K), and the absolute temperature (K).

The particular gas sensing behavior can be elaborated by n-n heterojunctions between ZnO and TiO_2. For TZ0.5 and TZ3, due to the large amount of ZnO and TiO_2 particles in each sample, the gas sensing behavior was controlled by the main phase in the sensing layer, so the TZ0.5 sensor behaved like a ZnO sensor while the TZ3 sensor behaved like a TiO_2 sensor. But in TZ1, the ZnO and TiO_2 amounts were similar to each other, so the function of the heterojunctions becomes the most important factor [48]. At the boundary of ZnO and TiO_2 particles, ZnO and TiO_2 formed a heterojunction, which led to a higher baseline resistance of TiO_2–ZnO (Fig. 12b) [49].

4. Conclusion

$Ti_3C_2T_x$ MXene was prepared from the Ti_3AlC_2 MAX phase by HF etching and stirring. ZnO nanoparticles were attached to the surface of $Ti_3C_2T_x$ by a simple hydrothermal method, and $Ti_3C_2T_x$ was oxidized by heat treatment to obtain TiO_2–ZnO composites. ZnO generated hydrothermally can be effectively attached to the surface of $Ti_3C_2T_x$ with the aid of CTAB. The majority of $Ti_3C_2T_x$ was oxidized to TiO_2 by heat treatment at 500 °C while the flake structure was preserved, according to XRD and XPS analysis.

Different ratios of TiO_2–ZnO sensors exhibited varied optimal operating temperatures and selectivity when tested the lung cancer biomarkers and significant interfering gases in exhaled human air. The response to 5 ppm isopropyl alcohol can reach 134.4% at 350 °C, which was lower than that of the ZnO-based sensor at optimal operating temperature. The TZ1 sensor had a distinct selectivity from TiO_2 and ZnO, and it had a similar response to isopropyl alcohol and formaldehyde, which was equivalent to having twofold selectivity for these two gases. Moreover, the gas sensing mechanism of TZ1 was studied, and the activation energy of TZ1 was the highest, which can account for the lower response than that of pure ZnO. Impressively, TZ1 can function properly in detecting low concentrations of VOCs with accuracy due to its low baseline noise and extensive operating temperature range. MXene with lower layer thickness and higher interlayer clearance may perform superior sensing performances due to higher specific surface area, which is our next step in material preparation optimization direction.

Declaration of competing interest

The authors declare that they have no known competing financial interests or personal relationships that could have appeared to influence the work reported in this paper.

Acknowledgements

This work is supported by the Outstanding Youth Foundation of Jiangsu Province of China under Grant No. BK20211548, Qinglan Project of Yangzhou University, Yangzhou Science and Technology Plan Project under Grant No. YZ2023246.

Appendix A. Supplementary data

Supplementary data to this article can be found online at https://doi.org/10.1016/j.ceramint.2024.02.095.

References

[1] B. Liu, H. Yu, X. Zeng, D. Zhang, J. Gong, L. Tian, J. Qian, L. Zhao, S. Zhang, R. Liu, Lung cancer detection via breath by electronic nose enhanced with a sparse group feature selection approach, Sens. Actuators, B 339 (2021) 129896, https://doi.org/10.1016/j.snb.2021.129896.
[2] G. Rocco, G. Pennazza, M. Santonico, F. Longo, R. Rocco, P. Crucitti, R. Antonelli Incalzi, Breathprinting and early diagnosis of lung cancer, J. Thorac. Oncol. 13 (2018) 883–894, https://doi.org/10.1016/j.jtho.2018.02.026.
[3] B. V A, M. Subramoniam, L. Mathew, Noninvasive detection of COPD and Lung Cancer through breath analysis using MOS Sensor array based e-nose, Expert Rev. Mol. Diagn. 21 (2021) 1223–1233, https://doi.org/10.1080/14737159.2021.1971079.
[4] Q. Wang, H. Wu, Y. Wang, J. Li, Y. Yang, X. Cheng, Y. Luo, B. An, X. Pan, E. Xie, Ex-situ XPS analysis of yolk-shell Sb_2O_3/WO_3 for ultra-fast acetone resistive sensor, J. Hazard Mater. 412 (2021) 125175, https://doi.org/10.1016/j.jhazmat.2021.125175.
[5] H. Park, J.-H. Kim, D. Vivod, S. Kim, A. Mirzaei, D. Zahn, C. Park, S.S. Kim, M. Halik, Chemical-recognition-driven selectivity of SnO_2-nanowire-based gas sensors, Nano Today 40 (2021) 101265, https://doi.org/10.1016/j.nantod.2021.101265.
[6] A.T. Guntner, V. Koren, K. Chikkadi, M. Righettoni, S.E. Pratsinis, E-nose sensing of low-ppb formaldehyde in gas mixtures at high relative humidity for breath screening of lung cancer? ACS Sens. 1 (2016) 528–535, https://doi.org/10.1021/acssensors.6b00008.

[7] A.A. Bagade, V.V. Ganbavle, S.V. Mohite, T.D. Dongale, B.B. Sinha, K.Y. Rajpure, Assessment of structural, morphological, magnetic and gas sensing properties of $CoFe_2O_4$ thin films, J. Colloid Interface Sci. 497 (2017) 181–192, https://doi.org/10.1016/j.jcis.2017.02.067.

[8] D.B. Patil, V.L. Patil, S.S. Patil, T.D. Dongale, N.D. Desai, P.R. Patil, R.M. Mane, P. N. Bhosale, P.S. Patil, P.M. Kadam, K.V. Khot, Facile synthesis of MoO_3 nanoplates based NO_2 gas sensor: ultra-selective and sensitive, Chem. Phys. Lett. 782 (2021) 139025, https://doi.org/10.1016/j.cplett.2021.139025.

[9] Z. Zheng, C. Zhang, Electronic noses based on metal oxide semiconductor sensors for detecting crop diseases and insect pests, Comput. Electron. Agric. 197 (2022) 106988, https://doi.org/10.1016/j.compag.2022.106988.

[10] Z. Song, J. Zhang, J. Jiang, Morphological evolution, luminescence properties and a high-sensitivity ethanol gas sensor based on 3D flower-like MoS_2–ZnO micro/nanosphere arrays, Ceram. Int. 46 (2020) 6634–6640, https://doi.org/10.1016/j.ceramint.2019.11.151.

[11] Y. Luo, A. Ly, D. Lahem, J.D.M. Martin, A.-C. Romain, C. Zhang, M. Debliquy, Role of cobalt in Co-ZnO nanoflower gas sensors for the detection of low concentration of VOCs, Sens. Actuators, B 360 (2022) 131674, https://doi.org/10.1016/j.snb.2022.131674.

[12] Y. Luo, A. Ly, D. Lahem, C. Zhang, M. Debliquy, A novel low-concentration isopropanol gas sensor based on Fe-doped ZnO nanoneedles and its gas sensing mechanism, J. Mater. Sci. 56 (2021) 3230–3245, https://doi.org/10.1007/s10853-020-05453-1.

[13] Y.-K. Syue, K.-C. Hsu, T.-H. Fang, C.-I. Lee, C.-J. Shih, Characteristics and gas sensor applications of ZnO-Perovskite heterostructure, Ceram. Int. 48 (2022) 12585–12591, https://doi.org/10.1016/j.ceramint.2022.01.126.

[14] V.L. Patil, S.A. Vanalakar, N.L. Tarwal, A.P. Patil, T.D. Dongale, J.H. Kim, P. S. Patil, Construction of Cu doped ZnO nanorods by chemical method for Low temperature detection of NO_2 gas, Sensor Actuator Phys. 299 (2019) 111611, https://doi.org/10.1016/j.sna.2019.111611.

[15] S.A. Vanalakar, M.G. Gang, V.L. Patil, T.D. Dongale, P.S. Patil, J.H. Kim, Enhanced gas-sensing response of zinc oxide nanorods synthesized via hydrothermal route for nitrogen dioxide gas, J. Electron. Mater. 48 (2019) 589–595, https://doi.org/10.1007/s11664-018-6752-1.

[16] Z. Li, Z. Yao, A.A. Haidry, Y. Luan, Y. Chen, B.Y. Zhang, K. Xu, R. Deng, N. Duc Hoa, J. Zhou, J.Z. Ou, Recent advances of atomically thin 2D heterostructures in sensing applications, Nano Today 40 (2021) 101287, https://doi.org/10.1016/j.nantod.2021.101287.

[17] J.Y. Park, Y. Kwak, H.-R. Lim, S.-W. Park, M.S. Lim, H.-B. Cho, N.V. Myung, Y.-H. Choa, Tuning the sensing responses towards room-temperature hypersensitive methanol gas sensor using exfoliated graphene-enhanced ZnO quantum dot nanostructures, J. Hazard Mater. 438 (2022) 129412, https://doi.org/10.1016/j.jhazmat.2022.129412.

[18] F. Meng, Z. Yang, Z. Yuan, H. Zhang, H. Zhu, Hydrothermal synthesis of CuO/rGO nanosheets for enhanced gas sensing properties of ethanol, Ceram. Int. 49 (2023) 5595–5603, https://doi.org/10.1016/j.ceramint.2022.10.174.

[19] F. Yin, Y. Li, W. Yue, S. Gao, C. Zhang, Z. Chen, Sn_3O_4/rGO heterostructure as a material for formaldehyde gas sensor with a wide detecting range and low operating temperature, Sens. Actuators, B 312 (2020) 127954, https://doi.org/10.1016/j.snb.2020.127954.

[20] M. Modak, S. Jagtap, Low temperature operated highly sensitive, selective and stable NO_2 gas sensors using N-doped SnO_2-rGO nanohybrids, Ceram. Int. 48 (2022) 19978–19989, https://doi.org/10.1016/j.ceramint.2022.03.273.

[21] P. Hao, Z. Lin, P. Song, Z. Yang, Q. Wang, rGO-wrapped porous $LaFeO_3$ microspheres for high-performance triethylamine gas sensors, Ceram. Int. 46 (2020) 9363–9369, https://doi.org/10.1016/j.ceramint.2019.12.194.

[22] A.V. Agrawal, R. Kumar, S. Venkatesan, A. Zakhidov, G. Yang, J. Bao, M. Kumar, M. Kumar, Photoactivated mixed in-plane and edge-enriched p-type MoS_2 flake-based NO_2 sensor working at room temperature, ACS Sens. 3 (2018) 998–1004, https://doi.org/10.1021/acssensors.8b00146.

[23] J.-S. Kim, H.-W. Yoo, H.O. Choi, H.-T. Jung, Tunable volatile organic compounds sensor by using thiolated ligand conjugation on MoS_2, Nano Lett. 14 (2014) 5941–5947, https://doi.org/10.1021/nl502906a.

[24] M. Naguib, M. Kurtoglu, V. Presser, J. Lu, J. Niu, M. Heon, L. Hultman, Y. Gogotsi, M.W. Barsoum, Two-dimensional nanocrystals produced by exfoliation of Ti_3AlC_2, Adv. Mater. 23 (2011) 4248–4253, https://doi.org/10.1002/adma.201102306.

[25] D. Zhang, S. Yu, X. Wang, J. Huang, W. Pan, J. Zhang, B.E. Meteku, J. Zeng, UV illumination-enhanced ultrasensitive ammonia gas sensor based on (001)TiO_2/MXene heterostructure for food spoilage detection, J. Hazard Mater. 423 (2022) 127160, https://doi.org/10.1016/j.jhazmat.2021.127160.

[26] W. Meng, X. Liu, H. Song, Y. Xie, X. Shi, M. Dargusch, Z.-G. Chen, Z. Tang, S. Lu, Advances and challenges in 2D MXenes: from structures to energy storage and conversions, Nano Today 40 (2021) 101273, https://doi.org/10.1016/j.nantod.2021.101273.

[27] M. Wu, M. He, Q. Hu, Q. Wu, G. Sun, L. Xie, Z. Zhang, Z. Zhu, A. Zhou, Ti_3C_2 MXene-based sensors with high selectivity for NH_3 detection at room temperature, ACS Sens. 4 (2019) 2763–2770, https://doi.org/10.1021/acssensors.9b01308.

[28] W. Chen, P. Li, J. Yu, P. Cui, X. Yu, W. Song, C. Cao, In-situ doping nickel single atoms in two-dimensional MXenes analogue support for room temperature NO_2 sensing, Nano Res. 15 (2022) 9544–9553, https://doi.org/10.1007/s12274-022-4904-3.

[29] T. Chen, W. Yan, Y. Wang, J. Li, H. Hu, D. Ho, SnS_2/MXene derived TiO_2 hybrid for ultra-fast room temperature NO_2 gas sensing, J. Mater. Chem. C 9 (2021) 7407–7416, https://doi.org/10.1039/D1TC00197C.

[30] Y. Yao, Y. Han, M. Zhou, L. Xie, X. Zhao, Z. Wang, N. Barsan, Z. Zhu, MoO_3/TiO_2/$Ti_3C_2T_x$ nanocomposite based gas sensors for highly sensitive and selective isopropanol detection at room temperature, J. Mater. Chem. A 10 (2022) 8283–8292, https://doi.org/10.1039/D1TA11018G.

[31] Y. Song, Y. Xu, Q. Guo, Z. Hua, F. Yin, W. Yuan, MXene-derived TiO_2 nanoparticles intercalating between RGO nanosheets: an assembly for highly sensitive gas detection, ACS Appl. Mater. Interfaces 13 (2021) 39772–39780, https://doi.org/10.1021/acsami.1c12154.

[32] M. Hou, J. Gao, L. Yang, S. Guo, T. Hu, Y. Li, Room temperature gas sensing under UV light irradiation for $Ti_3C_2T_x$ MXene derived lamellar TiO_2-C/g-C_3N_4 composites, Appl. Surf. Sci. 535 (2021) 147666, https://doi.org/10.1016/j.apsusc.2020.147666.

[33] Y. Zhou, Y. Wang, Y. Wang, H. Yu, R. Zhang, J. Li, Z. Zang, X. Li, MXene $Ti_3C_2t_x$-derived nitrogen-functionalized heterophase TiO_2 homojunctions for room-temperature trace ammonia gas sensing, ACS Appl. Mater. Interfaces 13 (2021) 56485–56497, https://doi.org/10.1021/acsami.1c17429.

[34] X. Tian, L. Yao, X. Cui, R. Zhao, T. Chen, X. Xiao, Y. Wang, A two-dimensional $Ti_3C_2T_x$ MXene@TiO_2/MoS_2 heterostructure with excellent selectivity for the room temperature detection of ammonia, J. Mater. Chem. A 10 (2022) 5505–5519, https://doi.org/10.1039/D1TA10773A.

[35] J. Wen, Z. Song, J. Ding, F. Wang, H. Li, J. Xu, C. Zhang, MXene-derived TiO_2 nanosheets decorated with Ag nanoparticles for highly sensitive detection of ammonia at room temperature, J. Mater. Sci. Technol. 114 (2022) 233–239, https://doi.org/10.1016/j.jmst.2021.12.005.

[36] S.J. Kim, H.-J. Koh, C.E. Ren, O. Kwon, K. Maleski, S.-Y. Cho, B. Anasori, C.-K. Kim, Y.-K. Choi, J. Kim, Y. Gogotsi, H.-T. Jung, Metallic $Ti_3C_2T_x$ MXene gas sensors with ultrahigh signal-to-noise ratio, ACS Nano 12 (2018) 986–993, https://doi.org/10.1021/acsnano.7b07460.

[37] M. Yang, T. Liang, Y. Peng, Q. Chen, Synthesis and characterization of a nanocomplex of ZnO nanoparticles attached to carbon nanotubes, Acta Phys. Chim. Sin. 23 (2007) 145–151, https://doi.org/10.1016/S1872-1508(07)60012-6.

[38] K. Wu, H. Chai, K. Xu, M. Debliquy, C. Zhang, Effect of {010} crystal facets of Bi_2MoO_6 and 1D/2D heterostructures for conductometric room temperature NH_3 gas sensors, Sens. Actuators, B 376 (2023) 132983, https://doi.org/10.1016/j.snb.2022.132983.

[39] H. Tai, Z. Duan, Z. He, X. Li, J. Xu, B. Liu, Y. Jiang, Enhanced ammonia response of $Ti_3C_2T_x$ nanosheets supported by TiO_2 nanoparticles at room temperature, Sens. Actuators, B 298 (2019) 126874, https://doi.org/10.1016/j.snb.2019.126874.

[40] R. Rella, J. Spadavecchia, M.G. Manera, S. Capone, A. Taurino, M. Martino, A. P. Caricato, T. Tunno, Acetone and ethanol solid-state gas sensors based on TiO_2 nanoparticles thin film deposited by matrix assisted pulsed laser evaporation, Sens. Actuators, B 127 (2007) 426–431, https://doi.org/10.1016/j.snb.2007.04.048.

[41] G.-J. Sun, H. Kheel, S. Park, S. Lee, S. Eon Park, C. Lee, Synthesis of TiO_2 nanorods decorated with NiO nanoparticles and their acetone sensing properties, Ceram. Int. 42 (2016) 1063–1069, https://doi.org/10.1016/j.ceramint.2015.09.031.

[42] C. Dong, X. Liu, B. Han, S. Deng, X. Xiao, Y. Wang, Nonaqueous synthesis of Ag-functionalized In_2O_3/ZnO nanocomposites for highly sensitive formaldehyde sensor, Sens. Actuators, B 224 (2016) 193–200, https://doi.org/10.1016/j.snb.2015.09.107.

[43] S.K. Charvadeh, S. Nejatinia, A.B. Khatibani, M.H. Ahmadi, Growth, characterization and investigation of gas-sensing performance of graphene and copper-doped zinc oxide prepared by sol–gel method, Bull. Mater. Sci. 45 (2022) 61, https://doi.org/10.1007/s12034-021-02644-7.

[44] S. Lenaerts, J. Roggen, G. Maes, FT-IR characterization of tin dioxide gas sensor materials under working conditions, Spectrochim. Acta 51 (1995) 883–894, https://doi.org/10.1016/0584-8539(94)01216-4.

[45] Y. Sun, B. Wang, B. Wang, Z. Zhao, W. Zhang, W. Zhang, K. Suematsu, J. Hu, Construction of flower-like PtO_x@ZnO/In_2O_3 hollow microspheres for ultrasensitive and rapid trace detection of isopropanol, ACS Appl. Mater. Interfaces 15 (2023) 12041–12051, https://doi.org/10.1021/acsami.2c20746.

[46] C. Zhang, Z. Zheng, K. Liu, M. Debliquy, Q. Liu, Highly sensitive and selective Sb_2WO_6 microspheres in detecting VOC biomarkers in cooked rice: experimental and density functional theory study, Food Chem. 424 (2023) 136323, https://doi.org/10.1016/j.foodchem.2023.136323.

[47] Y. Qin, X. Wang, J. Zang, Ultrasensitive ethanol sensor based on nano-Ag&ZIF-8 co-modified SiNWs with enhanced moisture resistance, Sens. Actuators, B 340 (2021) 129959, https://doi.org/10.1016/j.snb.2021.129959.

[48] X. Yang, Y. Deng, H. Yang, Y. Liao, X. Cheng, Y. Zou, L. Wu, Y. Deng, Functionalization of mesoporous semiconductor metal oxides for gas sensing: recent advances and emerging challenges, Adv. Sci. 10 (2023) 2204810, https://doi.org/10.1002/advs.202204810.

[49] Y. Xu, L. Zheng, C. Yang, W. Zheng, X. Liu, J. Zhang, Chemiresistive sensors based on core-shell ZnO@TiO_2 nanorods designed by atomic layer deposition for n-butanol detection, Sens. Actuators, B 310 (2020) 127846, https://doi.org/10.1016/j.snb.2020.127846.